Biophysical *Journal*
Biophysical Perspective

Biophysical Society

Out of the Randomness: Correlating Noise in Biological Systems

Maddalena Collini,[1,2] Margaux Bouzin,[1] and Giuseppe Chirico[1,2,*]
[1]Dipartimento di Fisica e Centro di Nanomedicina, Università degli Studi di Milano-Bicocca, Milan, Italy and [2]CNR-ISASI, Center for Complex Systems, Pozzuoli, Italy

ABSTRACT The study of the dynamics of biological systems requires one to follow relaxation processes in time with micron-size spatial resolution. This need has led to the development of different fluorescence correlation techniques with high spatial resolution and a tremendous (from nanoseconds to seconds) temporal dynamic range. Spatiotemporal information can be obtained even on complex dynamic processes whose time evolution is not forecast by simple Brownian diffusion. Our discussion of the most recent applications of image correlation spectroscopy to the study of anomalous sub- or superdiffusion suggests that this field still requires the development of multidimensional image analyses based on analytical models or numerical simulations. We focus in particular on the framework of spatiotemporal image correlation spectroscopy and examine the critical steps in getting information on anomalous diffusive processes from the correlation maps. We point out how a dual space-time correlative analysis, in both the direct and the Fourier space, can provide quantitative information on superdiffusional processes when these are analyzed through an empirical model based on intermittent active dynamics. We believe that this dual space-time analysis, potentially amenable to mathematical treatment and to the exact fit of experimental data, could be extended to include the rich phenomenology of subdiffusive processes, thereby quantifying relevant parameters for the various motivating biological problems of interest.

Complexity is an abused word. Even in scientific environments, we rarely use the term complex in a substantially different way than "difficult": difficult to predict and therefore to understand. Complexity is definitely not the simple random behavior of colloidal particles. A speckle pattern looks random but has features that are defined in terms of correlation functions and determined by the excitation source shape and by the emission fluctuations. Biological systems have or can display random features. But they also have the characteristic to be dynamic, either in a dynamic equilibrium or driven by a force out of the equilibrium state. The way DNA replicates, how it compacts and swells in the nucleus in the different cellular phases, the way it is repaired—all these examples of biological functions are intrinsically related to dynamics and to complexity. These mechanisms exemplify the dynamic behavior of an open dissipative system; the living cell, and within this, of the nucleus.

Jörg Langowski, who untimely passed away in May 2017, was attracted by the possibility to shed some light on these processes. By following his production, we can see distinctly that his aim was always to try to understand the molecular bases of the machinery involved in gene expression. His approach surfed on the crest of the evolution of fluctuation spectroscopy and imaging techniques while developing in the years his own analytical and simulative tools to rationalize the data (1–4). The latest developments from him and his colleagues (5) can offer us a perspective in future trends in the study not only of the cell nucleus in vivo but also of other complex molecular systems in biology. After the outline of Jörg's work, we will briefly review the theory and recent applications of fluctuation spectroscopy and imaging techniques, starting from photon correlation spectroscopy (PCS) up to the more recent image correlation spectroscopy (ICS).

Overview of fluctuation imaging techniques

Fluctuations in scattered light

Jörg's studies of DNA dynamics started with PCS (6) and were based on the use of coherent light and on the observation of the dynamics of the speckle pattern arising from the superposition of a high ($\sim 10^6$) number of scattering sources, whose average translational diffusion coefficient is D. Together with Mickey Schurr (7), he was one of the first to exploit PCS to sample the internal motion of supercoiled

Submitted December 27, 2017, and accepted for publication January 29, 2018.

*Correspondence: giuseppe.chirico@unimib.it

Editor: Anatoly Kolomeisky.
https://doi.org/10.1016/j.bpj.2018.01.034

DNA (8). The fluctuations were measured through the autocorrelation function (ACF) of the scattered intensity, which is related to the statistics of the molecular displacement according to the following equation:

$$\begin{aligned}\left\langle I\left(t+\tau,\overrightarrow{Q}\right)I\left(t,\overrightarrow{Q}\right)\right\rangle_t &= \left\langle I\left(t,\overrightarrow{Q}\right)\right\rangle_t^2\left(1+f_{coh}\left|\int d^3\overrightarrow{\Delta}_0 e^{i\overrightarrow{\Delta}_0\cdot\overrightarrow{Q}}P\left(\overrightarrow{\Delta}_0(\tau)\right)\right|^2\right)\\ &\propto\left\langle I\left(t,\overrightarrow{Q}\right)\right\rangle_t^2\left(1+f_{coh}exp\left(-\frac{\left|\overrightarrow{Q}\right|^2}{3}\left\langle\left|\overrightarrow{\Delta}_0(\tau)\right|^2\right\rangle\right)\right)\end{aligned}. \quad (1)$$

In writing Eq. 1 we assume a Gaussian distribution, $P(\vec{\Delta}_0(\tau))$, with zero mean for the displacement of the center of mass, $\vec{\Delta}_0(\tau)=\vec{r}(t+\tau)-\vec{r}(t)$. f_{coh} is a factor that accounts for the degree of coherence of the collected field, and the exchanged wave vector $\left|\vec{Q}\right|\cong\sin(\theta/2)/\lambda$ (where λ is the scattered light wavelength and θ is the scattering angle) determines the spatial resolution of the sampled dynamics. If the molecule is flexible, as DNA is, we have information on the normal modes of the chain in addition to center-of-mass diffusion. In this case, Eq. 1 is substituted in the experimental approaches by a heuristic functional form where a faster relaxation rate λ_{int} takes internal motions into account:

$$\left\langle I\left(t+\tau,\vec{Q}\right)I\left(t,\vec{Q}\right)\right\rangle_t\propto\left[\exp\left(-\left|\vec{Q}\right|^2D\tau\right)+b\exp\left(-\lambda_{int}\left(\left|\vec{Q}\right|^2\right)\tau\right)\right]^2. \quad (2)$$

The parameter b is related to the relative orientation of the excitation polarization and the emission analyzer. This was the analysis followed in the study of DNA molecules in vitro up to the '90s (9–11). It allowed for estimation of the internal motions of plectonemical supercoiled DNAs that were found to be faster than those of relaxed circular DNAs. However, that was clearly not the end of the story, and Jörg and other groups resorted to Monte Carlo (1,12,13) and Brownian dynamics (2,9,14–16) simulations. This was an unprecedented effort to access the DNA dynamics at a quantitative molecular level.

After the discovery of fluorescent proteins, the selectivity of the fluorescence signal compared to light scattering paved the way to the development of optical techniques allowing micron resolution and measurements in living cells. Times were ripening to merge the concepts of correlation spectroscopy and optical fluorescence microscopy (17,18).

Fluorescence correlation spectroscopy and ICS

The fluorescence signal F(t) from fluorescent particles changes with time because of the fluctuation of the number of particles N_{vol} within the excitation volume (such fluctuation was negligible in PCS, where $\langle N_{vol}\rangle\cong 10^6$). The average transit time of particles, because of Brownian diffusion, can be obtained as the decay time of the temporal ACF of the fluorescence fluctuations (19–21). Explicitly, the ACF is defined as

$$G(\tau)\equiv\frac{\langle\delta F(t+\tau)\delta F(t)\rangle_t}{\langle F(t)\rangle_t^2}, \quad (3)$$

where

$$\delta F(t)=\phi\int d\vec{x}MDE(\vec{x})\delta C(\vec{x},t) \quad (4)$$

is the fluorescence fluctuation, $\delta F(t)\equiv F(t)-\langle F(t)\rangle_t$, at time t (20,21) expressed in terms of the concentration fluctuation $\delta C(\vec{x},t)$. By assuming again a Gaussian $P(\vec{\Delta}_0(\tau))$ distribution, by substituting Eq. 4 into Eq. 3, and by converting the integration from the real to the Fourier space, we obtain the following (22):

$$G(\tau)\propto\int d\vec{Q}\exp\left(-\left|\vec{Q}\right|^2\frac{\left\langle\left|\vec{\Delta}_0(\tau)\right|^2\right\rangle}{6}\right)\left|\widehat{MDE}\left(\vec{Q}\right)\right|^2. \quad (5)$$

In Eq. 5, $\left\langle\left|\vec{\Delta}_0(\tau)\right|^2\right\rangle=6D\tau$ is the particles' mean-square displacement (MSD), and the exponential term in the kernel of the integral is the Fourier transform of the probability density function $P(\vec{\Delta}_0(\tau))$. Fluorescence correlation spectroscopy (FCS) averages such a probability density, measured by PCS at a single $\vec{Q}$ value, over a range of $\vec{Q}$ values determined by the objective numerical aperture and weighted over the frequency content of the molecular detection efficiency (MDE) function. If the MDE function is approximated by a three-dimensional Gaussian, $MDE(x,y,z)=MDE(0,0,0)\prod_{i=x,y,z}\exp(-2(\alpha/\omega_i)^2)$ (21), we obtain in terms of the one-dimensional MSD $\left\langle\left|\vec{\Delta}_{0,i=x,y,z}(\tau)\right|^2\right\rangle=\left\langle|i(t+\tau)-i(t)|^2\right\rangle=2D\tau$ (21,22):

$$\begin{aligned}G(\tau) &= \frac{1}{\langle N_{vol}\rangle}\prod_{i=x,y,z}\left(1+\frac{2\left\langle\left|\vec{\Delta}_{0,i}(\tau)\right|^2\right\rangle}{\omega_i^2}\right)^{-1/2}\\ &= \frac{1}{\langle N_{vol}\rangle}\prod_{i=x,y,z}\left(1+\frac{4D\tau}{\omega_i^2}\right)^{-1/2}.\end{aligned} \quad (6)$$

In summary, for a Gaussian distribution—$P(\vec{\Delta}_0(\tau))$—the ACF provides direct access to the distribution of the particle displacements through $\langle|\vec{\Delta}_{0,i}(\tau)|^2\rangle$. Indeed, $\langle|\vec{\Delta}_{0,i}(\tau)|^2\rangle$ can be directly obtained by numerical inversion of Eq. 6, as proposed in (23–25). FCS therefore complements single-particle tracking by not requiring ensemble averaging in terms of correlation functions, which allows for extraction of the statistics of complex stochastic transport processes by the measurement of single-particle trajectories (26–31).

Space is the additional variable needed when studying dynamic processes in living cells. By coupling single-point FCS and fluorescence microscopy, the correlation approach has been generalized into a variety of image-based techniques (ICS) (20,32,33) depending upon the timescale of the process of interest. ICS relies on the exploitation of the spatial and temporal information intrinsically encoded into (whole) images, either collected with camera-based detection on a total internal reflection or SPIM (single plane illumination) microscope (32,34,35) or acquired by raster scanning in a confocal or two-photon excitation setup (33,36–38). Excellent reviews on ICS techniques exist (32,33). We focus here on spatiotemporal ICS (STICS) (36) as the paradigm on which we discuss the general possibility to gain information on the statistics of the particle motion.

We define the STICS correlation map in terms of spatial, $(\xi,\eta)=\vec{\xi}$, and time, τ, lags as the following (36):

$$G(\vec{\xi},\tau) = \left\langle \frac{\langle \delta F(\vec{x}+\vec{\xi},t+\tau)\delta F(\vec{x},t)\rangle_{\vec{x}}}{\langle F(\vec{x},t)\rangle_{\vec{x}}\langle F(\vec{x},t+\tau)\rangle_{\vec{x}}}\right\rangle_t. \quad (7)$$

The spatiotemporal correlation function can be analytically derived for Brownian diffusion with the diffusion coefficient D and for the combination of two-dimensional (2D) diffusion and planar drift with velocity $\vec{v}=(v_x,v_y)$ (36). In the latter case, by assuming a diffusion equation of the type

$$\frac{\partial P(\vec{x},t)}{\partial t} = -\nabla(-D\nabla P(\vec{x},t)+\vec{v}P(\vec{x},t)) \quad (8)$$

and by operating in the Fourier space (x,y coordinates only), $G(\xi,\tau)$ can be computed as the following:

$$G(\vec{\xi},\tau)\propto\int d\vec{Q}\left|M\widehat{DE}(-\vec{Q})\right|^2 e^{-D|\vec{Q}|^2\tau+i\vec{Q}\cdot\vec{v}\tau}e^{-i\vec{Q}\cdot\vec{\xi}} \text{ and } \quad (9)$$

$$G(\vec{\xi},\tau)\propto\int d\vec{Q}\left|M\widehat{DE}(-\vec{Q})\right|^2 \times e^{-|\vec{Q}|^2\left(\left\langle|\vec{\Delta}_0(\tau)|^2\right\rangle-\left\langle\vec{\Delta}_0(\tau)\right\rangle^2\right)/4+i\vec{Q}\cdot\left\langle\vec{\Delta}_0(\tau)\right\rangle}e^{-i\vec{Q}\cdot\vec{\xi}}. \quad (10)$$

Equation 10 highlights that differently from single-point FCS (Eq. 6), the STICS correlation function provides an additional parameter, the space lag ξ, to access the first and second moment of the distribution of the particles' displacements. For the simple case described by Eq. 8, these are simply $\langle\vec{\Delta}_0(\tau)\rangle=\vec{v}\tau$ and $\langle|\vec{\Delta}_0(\tau)|^2\rangle-\langle\vec{\Delta}_0(\tau)\rangle^2=4D\tau$. This theoretical approach allows for measuring directly the MSD from the correlation maps as done recently, for example, by Gratton's group in STICS (39) and raster ICS (40).

A close result for Eq. 10 can then be obtained once the shape of the MDE is known (34,36). If a three-dimensional Gaussian is assumed, the resulting $G(\vec{\xi},\tau)$ is a 2D Gaussian in the $(\xi,\eta)=\vec{\xi}$ variables (36). The variance $\sigma^2(\tau)=(\omega^2_{i=x,y}+4D\tau)/2$ exclusively depends on the diffusion coefficient and increases linearly with the lag time τ. Information on the drift velocity can instead be gained from the coordinates of the maximum of the spatiotemporal correlation map: $(\xi_{max},\eta_{max})=(v_x,v_y)\tau/\delta x$ (δx being the image pixel size). In the case of wide-field SPIM images, the STICS correlation function can be approximated by a 2D Gaussian, with a variance dependent on the diffusion coefficient and velocity-dependent peak coordinates (34,41). Jörg, mainly together with Thorsten Wohland, worked out the details of FCS theory for point-wise measurement in SPIM setups (35) and applications to diffusion of proteins in cells. Our group recently worked out the STICS analysis of SPIM images (41), following their guidelines (34):

$$\begin{cases} G(\vec{\xi},\tau) = G_x(\xi,\tau)G_y(\eta,\tau)G_z(\tau) \\ G_z(\tau) = \dfrac{1}{M(\omega_z,D,\tau)} \\ G_x(\xi,\tau) = \displaystyle\sum_{k=0,1,2} h_k\left[x_k erf\left(\frac{x_k}{M(\omega_{xy},D,\tau)}\right)+\frac{M(\omega_{xy},D,\tau)}{\sqrt{\pi}}\exp\left(-\left(\frac{x_k}{M(\omega_{xy},D,\tau)}\right)^2\right)\right], \\ G_x(\eta,\tau) = \displaystyle\sum_{k=0,1,2} h_k\left[y_k erf\left(\frac{y_k}{M(\omega_{xy},D,\tau)}\right)+\frac{M(\omega_{xy},D,\tau)}{\sqrt{\pi}}\exp\left(-\left(\frac{y_k}{M(\omega_{xy},D,\tau)}\right)^2\right)\right] \end{cases} \quad (11)$$

where $M(\omega_i, D, \tau) = \sqrt{\omega_i^2 + 4D\tau}$, a is the pixel linear size, $\omega_{xy} = \omega_x = \omega_y$, and

$$\begin{cases} x_0 = a + (\xi + v_x\tau); & y_0 = a + (\eta + v_y\tau); & h_0 = 1 \\ x_1 = a - (\xi + v_x\tau); & y_1 = a - (\eta + v_y\tau); & h_1 = 1 \\ x_2 = (\xi + v_x\tau); & y_2 = (\eta + v_y\tau); & h_2 = -2 \end{cases}. \tag{12}$$

We finally observe that by defining

$$\widehat{G}(\vec{Q}, \tau) \equiv \left|M\widehat{D}E(-\vec{Q})\right|^2 \exp\left(-\left|\vec{Q}\right|^2\left(\left\langle\left|\vec{\Delta}_0(\tau)\right|^2\right\rangle - \left\langle\vec{\Delta}_0(\tau)\right\rangle^2\right)/4 + i\vec{Q}\cdot\left\langle\vec{\Delta}_0(\tau)\right\rangle\right), \tag{13}$$

Eq. 10 can be rewritten in the form $G(\vec{\xi}, \tau) \propto \int d\vec{Q}\widehat{G}(\vec{Q}, \tau)e^{-i\vec{Q}\cdot\vec{\xi}}$. $\widehat{G}(\vec{Q}, \tau)$ corresponds therefore to the 2D spatial Fourier transform of the $G(\vec{\xi}, \tau)$function. Whereas the derivation of $G(\vec{\xi}, \tau)$ requires a (possibly involved) integral over the $\vec{Q}$ variable, the analytical derivation is more straightforward for $\widehat{G}(\vec{Q}, \tau)$ (42). Instead of operating in the direct $\vec{\xi}$ space, it might therefore be convenient to move to the reciprocal space and adopt the formalism of k-space ICS (43).

Anomalous diffusion in biological systems: single-point and spot-variation FCS

Deviations from classical Brownian motion are common in the complex heterogeneous cellular environment (23,44). These deviations manifest themselves as a non-Gaussian diffusion propagator (45–48) and/or as a nonlinear time dependence of the particles' MSD, which exhibits an anomalous power-law increase of the type $MSD(t) = 4D_\alpha t^\alpha$ with $0 < \alpha < 2$, $\alpha \neq 1$ (23,44,49,50). Here, D_α is a generalized diffusion coefficient and α discriminates between sub- ($0 < \alpha < 1$) and superdiffusion ($1 < \alpha < 2$; for $\alpha = 1$ and $\alpha = 2$, classical Brownian motion and directed ballistic transport are retrieved, respectively).

Superdiffusion is generally ascribed to the molecular-motor-mediated active transport of tracer particles along the filaments of the cytoskeleton (Fig. 1). By contrast, the origin of intracellular subdiffusion is highly debated, being attributed to the complex topology of a crowded environment, to the temporary confinement of transmembrane proteins, and to the presence of rafts or corrals on variable submicrometric scales (Fig. 1) (25,51–54). Since anomalous diffusion is commonly encountered in the intracellular dynamics, there is the need for a generalization of the FCS and ICS theory capable of accounting for transport mechanisms more complex than normal diffusion.

A few attempts have been made to derive an extended FCS theory based on theoretical models of anomalous diffusion (53,55–58). The continuous-time random walk (CTRW) specifies p(x,t) in terms of two uncoupled probability density functions, $\lambda(|\underline{x}|)$ and $\psi(t)$, which regulate jump lengths and waiting times between successive jumps of the random walk (49,50). If a Gaussian distribution is maintained for $\lambda(|\underline{x}|)$ but an asymptotically fat-tailed distribution (a Lévy stable density) $\psi(t) \sim t^{-1-\mu}$ ($0 < \mu < 1$) is assumed for waiting times (44), particles can get stuck at a certain position for very long times: the system shows aging, ergodicity breaking, and subdiffusive time dependence for the MSD (49,50). Starting from a subdiffusive CTRW, a generalized diffusion equation of fractional order has been derived (44,59) and inserted into FCS theory (53). If we assume instead $\psi(t) = \delta(t - \tau)$ and a Lévy stable density $\lambda(|\underline{x}|)$ with index $0 < \mu < 2$, we obtain superdiffusive Lévy flights (49). The absence of a finite second moment for the step-length distribution prevents formal definition of an MSD, and a fractional μ exponent in the Fourier-transformed diffusion propagator (59) makes the inclusion of Lévy flights in the framework of FCS look unfeasible. In the attempt of regularizing the second-moment divergence, a cutoff in the jump length distribution (truncated Lévy

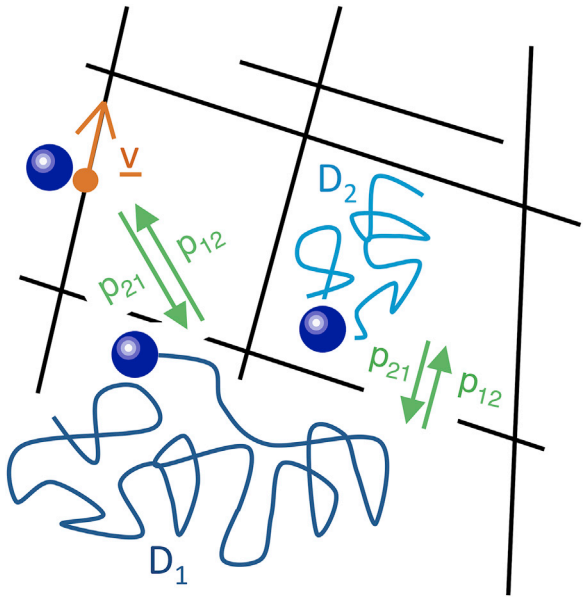

FIGURE 1 Schematic representation of intracellular sub- and superdiffusion. Permeable and impermeable barriers (*black lines*) represent both phase separations and physical obstacles as well as separate regions where particles have different diffusion constants. Subdiffusion occurs when a particle (*large blue sphere*) undergoing Brownian diffusion with the diffusion coefficient D_1 overcomes a barrier with the given probability p_{12}, thereby entering an adjacent domain where it diffuses with the diffusion coefficient D_2 (and vice versa). In a subdiffusive scenario, symmetrically permeable ($p_{12} = p_{21} \neq 0$) barriers and identical diffusion coefficients D_1 and D_2 are usually exploited to describe hindered diffusion in a meshwork of filaments; randomly located and isolated closed fences with asymmetric probabilities $p_{12} \neq p_{21}$ have instead been adopted to describe dynamic partitioning and transient or permanent trapping of tracer particles into sparse domains. If the diffusing particle reaches a binding partner (*small orange dot*, representing, e.g., a molecular motor protein) and is actively transported along a barrier with drift velocity $\vec{v}$, superdiffusion is encountered instead. p_{12} and p_{21} are related here to the binding and unbinding rates, and phases of normal diffusion (D_1) alternate with phases of directed transport ($D_1 + \vec{v}$). To see this figure in color, go online.

flights) and a spatiotemporal coupling between $\lambda(|\underline{x}|)$ and $\psi(t)$ aimed at penalizing long jumps (Lévy walks) have been proposed (31,60,61).

Anomalous dynamics in slowly fluctuating, inhomogeneous environments with linear MSD(t) and a non-Gaussian short-time displacement probability density function have been treated with superstatistical approaches (45,48,62). In the "diffusing diffusivity" model, non-Gaussian diffusion is attributed to the convolution of elementary Gaussian processes (62,63), with a time-varying diffusivity whose distribution satisfies the random-walk advection-diffusion equation (63).

The alternative approach of time-dependent diffusion coefficients (TDDCs) (55,64) appears more easily transferable to the FCS context. Exploited by fractional Brownian motion to introduce correlations between particle displacements (56), TDDCs directly obtained from the power-law scaling of the MSD (55) allow for deriving the FCS correlation function (52,54,55,65) as

$$G(\tau) = \frac{1}{\langle N_{vol}\rangle}\prod_{i=x,y,z}\left(1+\left(\frac{4D\tau}{\omega_i^2}\right)^{\alpha}\right)^{-1/2}. \qquad (14)$$

However, identification of the real underlying subdiffusion mechanism remains ambiguous. A multicomponent Brownian diffusion model often provides a similarly satisfactory fit of experimental correlation functions (64–66), and ACFs derived with TDDCs appear similar to numerically simulated ACFs in the presence of a CTRW with fat-tailed $\psi(t)$ distribution (54). Moreover, the ACF curves do not always catch the diffusion anomaly on the proper spatiotemporal scale, especially when a crossover from anomalous to linear time dependence is observed for the MSD (24,52,67,68). In this context, an approach based on spot variation (or variable lengthscale) FCS (sv-FCS) has been proposed (24,68).

In sv-FCS, a plot of the correlation half-height decay time, $\tau_{1/2}$, versus the observation area ω_{xy}^2 ($\omega_x^2 = \omega_y^2 \equiv \omega_{xy}^2$) is obtained by progressively altering ω_{xy}^2 (51,68). For Brownian diffusion, $\tau_{1/2}$ is directly proportional to ω_{xy}^2, whereas for anomalous subdiffusion, different linear regimes are observed (typically when ω_{xy}^2 is at least a few times the typical obstacle or mesh size). The nonzero extrapolated intercept offers insight into the diffusion anomaly: a positive intercept is indicative of confinement into sparse microdomains, and a negative one is found for particles trapping in a meshwork (68). When combined with a numerical inversion procedure of experimental ACFs, sv-FCS also allows for extracting the particles' MSD under the assumption of a Gaussian propagator (24). However, the only available analytical derivation covers the case of particles diffusing in a periodic, meshwork-like structure (69): conclusions on the positive and negative intercept of the FCS diffusion law are almost exclusively based on numerical Monte Carlo simulations (51,68), and to our knowledge, no application of FCS diffusion laws to superdiffusion has been reported.

STICS analysis as a variable-length ICS

The results of sv-FCS stress the importance of a spatially extended correlation analysis and suggest moving to image-based correlation methods for the investigation of complex transport mechanisms.

Subdiffusive motions

Starting from the analysis of the general relation between the STICS map and the MSD (Eq. 10), we envision a general framework for the retrieval of information on the displacement statistics. Experimentally, we assume to fit the STICS maps to a Gaussian trial function; theoretically, we derive the displacement of the map maximum from the center of the correlation space and its $1/e^2$ halfwidth from the second-order expansion of the map:

$$\begin{cases} \left.\dfrac{\partial G_x(\xi,\tau)}{\partial\xi}\right|_{\xi_{max}} = 0 \\ \dfrac{1}{\sigma_\xi^2(\tau)} = \dfrac{1}{G_x(\xi_{max},\tau)}\left.\dfrac{\partial^2 G_x(\xi,\tau)}{\partial^2\xi}\right|_{\xi_{max}} \end{cases}. \qquad (15)$$

We can derive similarly the width of the correlation map in the η direction and the overall width as $\sigma_G^2(\tau) = \sigma_\xi^2(\tau) + \sigma_\eta^2(\tau)$. For SPIM microscopy images, we obtain the following (41):

$$\begin{cases} \xi_{max} = -v_x\tau \\ \eta_{max} = -v_y\tau \\ \sigma_G^2(\tau) = \dfrac{\sqrt{\pi}}{2}\dfrac{a^2}{\beta^2\left(1-e^{-\beta^2}\right)}\left[\beta Erf(\beta) + \dfrac{1}{\sqrt{\pi}}\left(e^{-\beta^2}-1\right)\right] \end{cases}. \qquad (16)$$

In Eq. 16 $\beta = a\Big/\sqrt{\omega_{i=x,y}^2 + 4D_\alpha\tau^\alpha}$ accounts for a possible subdiffusion through the exponent $0 < \alpha \leq 1$, and Erf() is the error function. STICS maps have been simulated (Eq. 11) with $\vec{v} = (0,0)$ as a function of the diffusion coefficient, the pixel size, and the anomaly parameter. In SPIM detection, the pixel size can be changed in the postprocessing phase by rebinning the images, thereby providing a software version of the spot variation technique (18,70).

The Gaussian approximation (Eq. 16) can fit well the simulated maps (Fig. 2, *A* and *B*): the effect of the anomaly is to widen the width as α decreases. The fit of the lag time dependence of $\sigma_G^2(\tau)$ to Eq. 16 allows for retrieving the anomaly parameter with good accuracy even when the $\sigma_G^2(\tau)$ plot is reconstructed at low temporal resolution (~10 Hz, Fig. 2 *B*, *short-dashed lines* and *inset*). When

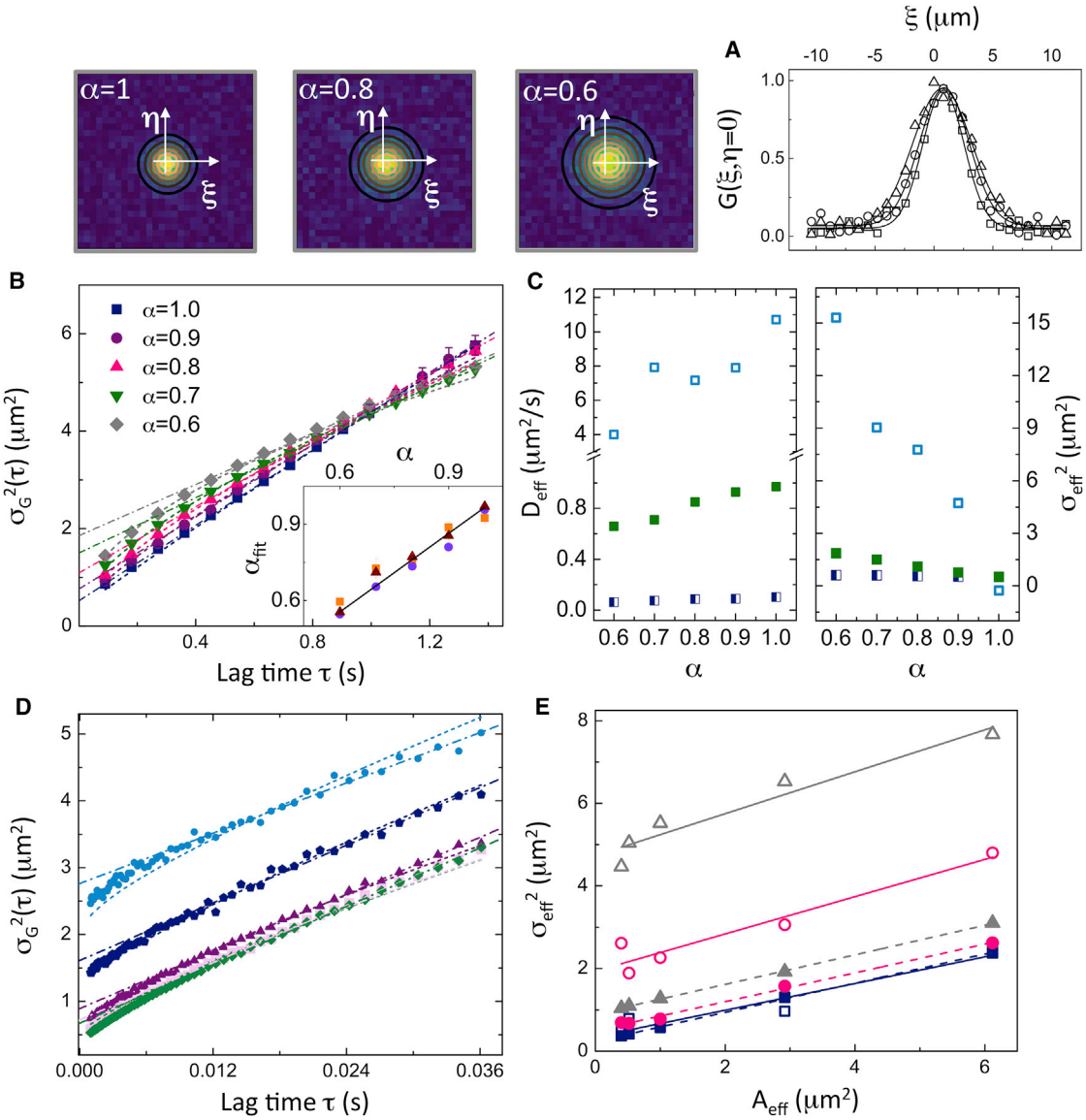

FIGURE 2 STICS analysis of anomalous diffusion. (*A*) Shown are STICS correlation functions simulated at $\tau = 136$ ms for $D_\alpha = 10\ \mu m^2/s^\alpha$; $\alpha = 1$, 0.8, and 0.6; and $\omega_{xy} = a = 0.6\ \mu m$. Normalized $G(\xi,\eta = 0)$ profiles are reported with the best Gaussian fit (*squares*: $\alpha = 1$; *circles*: $\alpha = 0.8$; and *triangles*: $\alpha = 0.6$). (*B*) Shown is the variance $\sigma_G^2(\tau)$ recovered from the Gaussian fit of the STICS maps for $D_\alpha = 1\ \mu m^2/s^\alpha$, $0.6 < \alpha < 1$, and $\omega_{xy} = a = 0.6\ \mu m$. Short dashed lines fit to Eq. 16 with $D_{fit} = 1.3 \pm 0.2\ \mu m^2/s$, and $\alpha_{fit} = 0.94 \pm 0.02$, 0.89 ± 0.02, 0.76 ± 0.03, 0.73 ± 0.04, and 0.60 ± 0.01 for $\alpha = 1$, 0.9, 0.8, 0.7, and 0.6, respectively. Dashed-dotted lines fit to $\sigma_{eff}^2 + 4D_{eff}\tau$ for $\tau > 400$ ms (fit parameters in (*C*)). Inset: α_{fit} recovered from the fit of $\sigma_G^2(\tau)$ to Eq. 16 for $D_\alpha = 0.1$, 1, and 10 $\mu m^2/s^\alpha$ (*squares*, *circles*, *triangles*). The solid line is $\alpha_{fit} = 1.03\ (\pm 0.02)\ \alpha$. (*C*) Shown are σ_{eff}^2 (*right*) and D_{eff} (*left*) as a function of α, for $D_\alpha = 10$, 1, and 0.1 $\mu m^2/s^\alpha$(*open squares*, *filled squares*, and *half-filled squares*) with $\omega_{xy} = a = 0.6\ \mu m$ ($A_{eff}^2 = a^2 + \omega_{xy}^2 = 0.72\ \mu m^2$). (*D*) $\sigma_G^2(\tau)$ for $D_\alpha = 10\ \mu m^2/s^\alpha$, $\alpha = 0.8$, and $\omega_{xy} = 0.8\ \mu m$, and variable pixel size is shown: a = 0.2 (*diamonds*), 0.4 (*squares*), 0.8 (*triangles*), 1.6 (*pentagons*), and 2.4 (*circles*) μm. Short dashed lines fit to Eq. 16; dashed-dotted lines show linear fit to $\sigma_{eff}^2 + 4D_{eff}\tau$ for $\tau > 8$ ms. (*E*) σ_{eff}^2 versus A_{eff}^2 for $D_\alpha = 1\ \mu m^2/s^\alpha$(*filled symbols*), and $D_\alpha = 10\ \mu m^2/s^\alpha$ (*open symbols*) for $\alpha = 1.0$ (*squares*), 0.8 (*circles*), and 0.6 (*triangles*); solid and dashed lines show linear fit of the data for $D_\alpha = 10$ and 1 $\mu m^2/s^\alpha$. 3% of Gaussian noise was added to all the simulated STICS maps. To see this figure in color, go online.

the short lag time part of the curve is not accessible, a linear fit $\sigma_G^2(\tau) = \sigma_{eff}^2 + 4D_{eff}\tau$ (Fig. 2 *B*, *dot-dashed lines*) provides an effective diffusion coefficient D_{eff} and an effective width σ_{eff}^2 (Fig. 2 *C*). D_{eff} decreases for a decreasing anomaly parameter, and for $1 \geq \alpha \geq 0.8$, the difference between D_{eff} and D_α is at most 15%. σ_{eff}^2 increases as α decreases, confirming the visual inspection of the STICS maps shown in Fig. 2 *A*. In general, we find that $\sigma_{eff}^2 > \sigma_{eff,\alpha=1}^2$ in the presence of anomalous diffusion: therefore, the value of σ_{eff}^2 measured for a fixed value of the pixel size can provide indication of a diffusion anomaly.

This indication is reinforced by computing the STICS maps at different values of the effective sampling area $A_{eff}^2 = a^2 + \omega_{xy}^2$, obtained by binning the pixels of the images of the same xyt- stack. The obtained $\sigma_G^2(\tau)$-versus-τ plot (Fig. 2 *D*) is linear at long lag times, with an increasing

intercept at increasing pixel size. Fig. 2 *E* summarizes the dependence of σ^2_{eff}on $A_{eff}{}^2$ (for fixed ω_{xy}) at a different anomaly parameter and diffusion coefficient. When $\alpha = 1$, the σ^2_{eff}-versus $A_{eff}{}^2$ -plot is linear for a $> \omega_{xy}$ (Eq. 16 with $\tau = 0$), with the slope being fully determined by ω_{xy}. When $\alpha \neq 1$, σ^2_{eff} always lies above the normal diffusion curve. This behavior can be exploited, as done in Fig. 2 *C*, to put into evidence the presence of an anomaly on the diffusion.

In summary, the study of the dependence of the STICS map on the lag time and on the effective sampling area can be advantageously employed to point out the presence of a subdiffusive anomaly. As a limitation of the approach, quantitative extraction of the α parameter requires the knowledge of the diffusion coefficient, which is not always known a priori. Moreover, the α parameter does not provide a full picture of the phenomenology of the process under study.

Superdiffusive motions

In the presence of superdiffusion, it is more convenient to monitor the correlation peak coordinates (ξ_{max}, η_{max}) as a function of the lag time. This can be appreciated by working on simulated Lévy trajectories for increasing values of the exponent μ of the jump-length distribution $\lambda(|\underline{x}|) \sim |\underline{x}|^{-1-\mu}$. Starting from these trajectories, we have simulated and analyzed by the STICS formalism time sequences of images of noninteracting particles undergoing Lévy flight superdiffusion. As reported in Fig. 3, *A* and *B*, a nonlinear time dependence of the STICS peak displacement is obtained, becoming more and more pronounced as the exponent μ decreases. A linear relation (ξ_{max}, η_{max}) $\delta x = (v_x, v_y)\tau$ is expected for directed motion with planar drift velocity $\vec{v}$, whereas no displacement of the STICS maximum should be retrieved for subnormal or normal diffusion (36). Therefore, the irregular (ξ_{max}, η_{max})-versus-τ plot could be used as an indication of the underlying superdiffusive behavior of the simulated Lévy flights. However, since an analytical description of the (ξ_{max}, η_{max})-versus-τ plot in terms of the exponent μ is prevented by the complex diffusion propagator associated with Lévy flights (59), conclusions on the possible value of the μ exponent can at most be drawn based on the comparison with the results of numerical simulations.

A different analytical framework, aimed at the investigation of enhanced diffusion by correlation spectroscopy, has been recently developed by our group (42) in terms of an

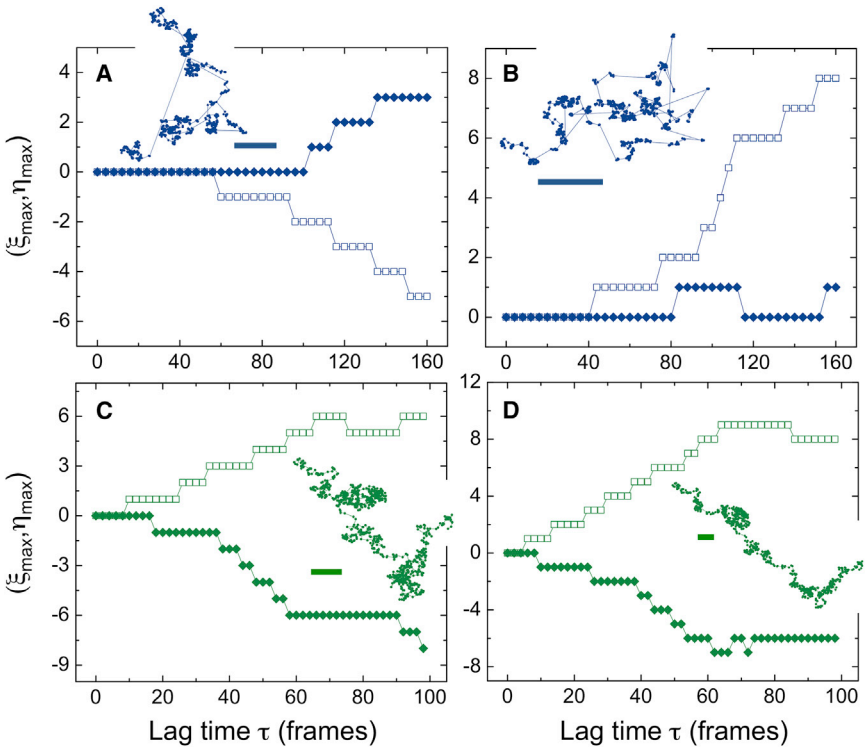

FIGURE 3 STICS analysis of superdiffusion. (*A* and *B*) Peak coordinates ξ_{max} and η_{max} (*filled and open symbols*, in pixel units) versus the lag time τ provided by the STICS analysis of simulated single-particle Lévy flights (reported as *insets* with a 10-pixel scale bar representing 1000 steps of total trajectory length) of index $\mu = 1.5$ (*A*) and $\mu = 1.3$ (*B*). For the generation of Lévy-type trajectories, at each time point the particle direction and jump length have been extracted as pseudorandom numbers from a uniform distribution in the interval $(0,2\pi)$ and from a Lévy stable distribution of index μ. Image temporal stacks have been produced by convolving the particle coordinates with a 2D Gaussian function (four-pixel e^{-2} radius) to simulate the microscope point-spread function. (*C* and *D*) (ξ_{max},η_{max})-versus-τ plot (ξ_{max} (*filled symbols*) and η_{max} (*open symbols*), in pixel units) recovered from the STICS analysis of single-particle trajectories simulated according to the two-state intermittent dynamics of Eq. 17, with $D = 2 \times 10^{-4}$ $\mu m^2/s$, $|\underline{v}| = 2 \times 10^{-3}$ $\mu m/s$, drift direction angle = 330°, and $p_{21} = 0.05$; $p_{12} = 0.05$ in (*C*) and $p_{12} = 0.5$ in (*D*), leading to an equilibrium probability for the diffusion plus drift state $P_2{}^{eq} = 0.5$ in (*C*) and $P_2{}^{eq} = 0.9$ in (*D*). Following the procedure reported in (42) for the generation of trajectories, the sequence of state occupancies has been generated as a discrete Markov chain based on the occupation state at t_{i-1} and on the comparison of the probabilities p_{12} and p_{21} with a pseudorandom number extracted at the same time step t_i in the interval (0,1). Then the state sequence has been employed to define particle displacements: the length and direction of Brownian jumps have been extracted from a Gaussian distribution with zero mean and variance $2D\Delta t$ and from a uniform distribution in the range $(0,2\pi)$; for the particle in state 2, a term $v\Delta t$ has been added to the Brownian displacement. Trajectories are reported as insets with a 10-pixel scale bar; a pixel size $\delta x = 0.03$ μm and a time step $\Delta t = 2.5$ s have been adopted for the simulations. D and $|\underline{v}|$ values chosen for the simulations are in agreement with the experimental findings in (42). To see this figure in color, go online.

intermittent model in which phases of 2D Brownian diffusion (with diffusion coefficient D) alternate with phases of active, directed transport (D and planar drift velocity$\vec{v}$) (71). Occupation probabilities for the two states, p_{12} and p_{21}, are assigned by the corresponding transition rates k_{12} and k_{21}. The two-state model can be schematically represented as

$$D \underset{k_{21}}{\overset{k_{12}}{\rightleftharpoons}} D + \underline{v}. \tag{17}$$

The equivalence between the two approaches in terms of nonlinear (ξ_{max}, η_{max})-versus-τ plots has been evaluated by numerical simulations (Fig. 3, *C* and *D*). The adoption of the model described by Eq. 17 allows for solving the Fick's equation for the diffusing and drifting populations and for incorporating such a solution in the derivation of correlation functions in the reciprocal Fourier (k,τ) space (42), thereby exploiting the formalism of k-space ICS (43). This approach provides a quantitative estimate of the transport parameters and the transition rates of the intermittent dynamics (42).

Perspective

The discussion of these few selected examples, together with the output of the simulations of the STICS maps, indicates that there is a strong need for new image analysis methods to address the complexity of a multitude of processes in the crowded and intricate cellular environment. Future developments in this field should allow for bringing super- and subdiffusion into evidence, starting from a spatiotemporal monitoring of the cells, and for casting the analysis of the variety of possible situations (meshwork confinement, crowding, microdomain partitioning, etc.) in a general framework. In the case of superdiffusion, a relatively simple approach obtained with the intermittent model of Eq. 17 has been analytically solved in the Fourier space (42), quantifying the relevant transport properties associated with the model. In the case of subdiffusion, the situation seems to not be solved yet: the large majority of data require comparison to simulations, and based on those, approximate expressions have been derived for the STICS variance in the presence of dynamic partitioning and meshworks (39). Future developments should encompass the development of models for subdiffusion based on the a priori knowledge of the molecular cell biology (see Fig. 1), equivalent to the phenomenological intermittent model for superdiffusion. Such models should comprise parameters such as the distribution and size of obstacles, the tracers' diffusion coefficient in the different compartments, and the confinement probabilities. The analytical incorporation of these models in the framework of ICS should be easier, or exclusively possible, in the reciprocal space by Fourier transforming the STICS map in the spatial coordinates.

AUTHOR CONTRIBUTIONS

G.C., M.C., and M.B. all equally contributed to the writing of the manuscript and to the numerical simulations.

ACKNOWLEDGMENTS

We acknowledge the funding from Università degli Studi di Milano-Bicocca for the year 2017.

REFERENCES

1. Hammermann, M., N. Brun, …, J. Langowski. 1998. Salt-dependent DNA superhelix diameter studied by small angle neutron scattering measurements and Monte Carlo simulations. *Biophys. J.* 75:3057–3063.
2. Klenin, K., H. Merlitz, and J. Langowski. 1998. A Brownian dynamics program for the simulation of linear and circular DNA and other wormlike chain polyelectrolytes. *Biophys. J.* 74:780–788.
3. Fritsch, C. C., and J. Langowski. 2011. Chromosome dynamics, molecular crowding, and diffusion in the interphase cell nucleus: a Monte Carlo lattice simulation study. *Chromosome Res.* 19:63–81.
4. Kühn, T., T. O. Ihalainen, …, J. Timonen. 2011. Protein diffusion in mammalian cell cytoplasm. *PLoS One.* 6:e22962.
5. Langowski, J. 2017. Single plane illumination microscopy as a tool for studying nucleome dynamics. *Methods.* 123:3–10.
6. Pecora, R. 1985. Dynamic Light Scattering: Applications of Photon Correlation Spectroscopy. Springer, New York.
7. Schurr, J. M., and K. S. Schmitz. 1986. Dynamic light scattering studies of biopolymers: Effects of charge, shape, and flexibility. *Annu. Rev. Phys. Chem.* 37:271–305.
8. Langowski, J., A. S. Benight, …, U. Schomburg. 1985. Change of conformation and internal dynamics of supercoiled DNA upon binding of Escherichia coli single-strand binding protein. *Biochemistry.* 24:4022–4028.
9. Hammermann, M., C. Steinmaier, …, J. Langowski. 1997. Salt effects on the structure and internal dynamics of superhelical DNAs studied by light scattering and Brownian dynamics. *Biophys. J.* 73:2674–2687.
10. Langowski, J., W. Kremer, and U. Kapp. 1992. Dynamic light scattering for study of solution conformation and dynamics of superhelical DNA. *Methods Enzymol.* 211:430–448.
11. Chirico, G., and G. Baldini. 1989. Dynamic light scattering from DNA plasmids: Diffusional and internal motion. *J. Mol. Liq.* 41:327–345.
12. Gebe, J. A., S. A. Allison, …, J. M. Schurr. 1995. Monte Carlo simulations of supercoiling free energies for unknotted and trefoil knotted DNAs. *Biophys. J.* 68:619–633.
13. Langowski, J., U. Kapp, …, A. Vologodskii. 1994. Solution structure and dynamics of DNA topoisomers: Dynamic light scattering studies and Monte Carlo simulations. *Biopolymers.* 34:639–646.
14. Chirico, G., and J. Langowski. 1996. Brownian dynamics simulations of supercoiled DNA with bent sequences. *Biophys. J.* 71:955–971.
15. Merlitz, H., K. Rippe, …, J. Langowki. 1998. Looping dynamics of linear DNA molecules and the effect of DNA curvature: a study by Brownian dynamics simulation. *Biophys J.* 74:773–779.
16. Chirico, G., and J. Langowski. 1994. Kinetics of DNA supercoiling studied by Brownian dynamics simulation. *Biopolymers.* 34:415–433.
17. Koppel, D. E., D. Axelrod, …, W. W. Webb. 1976. Dynamics of fluorescence marker concentration as a probe of mobility. *Biophys. J.* 16:1315–1329.
18. Weidemann, T., J. Mücksch, and P. Schwille. 2014. Fluorescence fluctuation microscopy: a diversified arsenal of methods to investigate molecular dynamics inside cells. *Curr. Opin. Struct. Biol.* 28:69–76.

19. Magde, D., E. L. Elson, and W. W. Webb. 1974. Fluorescence correlation spectroscopy. II. An experimental realization. *Biopolymers.* 13:29–61.

20. Elson, E. L. 2011. Fluorescence correlation spectroscopy: past, present, future. *Biophys. J.* 101:2855–2870.

21. Schwille, P. 2001. Fluorescence correlation spectroscopy and its potential for intracellular applications. *Cell Biochem. Biophys.* 34: 383–408.

22. Krichevsky, O., and G. Bonnet. 2002. Fluorescence correlation spectroscopy: the technique and its applications. *Rep. Prog. Phys.* 65: 251–297.

23. Höfling, F., and T. Franosch. 2013. Anomalous transport in the crowded world of biological cells. *Rep. Prog. Phys.* 76:046602.

24. Banks, D. S., C. Tressler, …, C. Fradin. 2016. Characterizing anomalous diffusion in crowded polymer solutions and gels over five decades in time with variable-lengthscale fluorescence correlation spectroscopy. *Soft Matter.* 12:4190–4203.

25. Horton, M. R., F. Höfling, …, T. Franosch. 2010. Development of anomalous diffusion among crowding proteins. *Soft Matter.* 6:2648–2656.

26. Norregaard, K., R. Metzler, …, L. B. Oddershede. 2017. Manipulation and motion of organelles and single molecules in living cells. *Chem. Rev.* 117:4342–4375.

27. Weigel, A. V., B. Simon, …, D. Krapf. 2011. Ergodic and nonergodic processes coexist in the plasma membrane as observed by single-molecule tracking. *Proc. Natl. Acad. Sci. USA.* 108:6438–6443.

28. Jeon, J. H., V. Tejedor, …, R. Metzler. 2011. In vivo anomalous diffusion and weak ergodicity breaking of lipid granules. *Phys. Rev. Lett.* 106:048103.

29. Tabei, S. M. A., S. Burov, …, N. F. Scherer. 2013. Intracellular transport of insulin granules is a subordinated random walk. *Proc. Natl. Acad. Sci. USA.* 110:4911–4916.

30. Meroz, Y., and I. M. Sokolov. 2015. A toolbox for determining subdiffusive mechanisms. *Phys. Rep.* 573:1–29.

31. Metzler, R., J. H. Jeon, …, E. Barkai. 2014. Anomalous diffusion models and their properties: non-stationarity, non-ergodicity, and ageing at the centenary of single particle tracking. *Phys. Chem. Chem. Phys.* 16:24128–24164.

32. Bag, N., and T. Wohland. 2014. Imaging fluorescence fluctuation spectroscopy: new tools for quantitative bioimaging. *Annu. Rev. Phys. Chem.* 65:225–248.

33. Digman, M. A., and E. Gratton. 2011. Lessons in fluctuation correlation spectroscopy. *Annu. Rev. Phys. Chem.* 62:645–668.

34. Krieger, J. W., A. P. Singh, …, T. Wohland. 2015. Imaging fluorescence (cross-) correlation spectroscopy in live cells and organisms. *Nat. Protoc.* 10:1948–1974.

35. Krieger, J. W., A. P. Singh, …, J. Langowski. 2014. Dual-color fluorescence cross-correlation spectroscopy on a single plane illumination microscope (SPIM-FCCS). *Opt. Express.* 22:2358–2375.

36. Hebert, B., S. Costantino, and P. W. Wiseman. 2005. Spatiotemporal image correlation spectroscopy (STICS) theory, verification, and application to protein velocity mapping in living CHO cells. *Biophys. J.* 88:3601–3614.

37. Digman, M. A., C. M. Brown, …, E. Gratton. 2005. Measuring fast dynamics in solutions and cells with a laser scanning microscope. *Biophys. J.* 89:1317–1327.

38. Sironi, L., M. Bouzin, …, G. Chirico. 2014. In vivo flow mapping in complex vessel networks by single image correlation. *Sci. Rep.* 4:7341.

39. Di Rienzo, C., E. Gratton, …, F. Cardarelli. 2013. Fast spatiotemporal correlation spectroscopy to determine protein lateral diffusion laws in live cell membranes. *Proc. Natl. Acad. Sci. USA.* 110: 12307–12312.

40. Di Rienzo, C., V. Piazza, …, F. Cardarelli. 2014. Probing short-range protein Brownian motion in the cytoplasm of living cells. *Nat. Commun.* 5:5891.

41. Ceffa, N. G., M. Bouzin, …, G. Chirico. 2018. Spatiotemporal image correlation analysis for 3D flow field mapping in microfluidic devices. *Anal. Chem.* 90:2277–2284.

42. Bouzin, M., L. Sironi, …, M. Collini. 2015. An intermittent model for intracellular motions of gold nanostars by k-space scattering image correlation. *Biophys. J.* 109:2246–2258.

43. Kolin, D. L., D. Ronis, and P. W. Wiseman. 2006. k-Space image correlation spectroscopy: a method for accurate transport measurements independent of fluorophore photophysics. *Biophys. J.* 91:3061–3075.

44. Metzler, R., and J. Klafter. 2004. The restaurant at the end of the random walk: recent developments in the description of anomalous transport by fractional dynamics. *J. Phys. A Math. Gen.* 37:R161–R208.

45. Wang, B., J. Kuo, …, S. Granick. 2012. When Brownian diffusion is not Gaussian. *Nat. Mater.* 11:481–485.

46. Jeon, J., M. Javanainen, …, I. Vattulainen. 2016. Protein crowding in lipid bilayers gives rise to non-Gaussian anomalous lateral diffusion of phospholipids and proteins. *Phys. Rev. X.* 6:021006.

47. Lampo, T. J., S. Stylianidou, …, A. J. Spakowitz. 2017. Cytoplasmic RNA-protein particles exhibit non-Gaussian subdiffusive behavior. *Biophys. J.* 112:532–542.

48. Ślezak, J., R. Metzler, and M. Magdziarz. 2017. Superstatistical generalized Langevin equation: non-Gaussian viscoelastic anomalous diffusion. *New J. Phys.* 20:023026.

49. Metzler, R., A. V. Chechkin, and J. Klafter. 2009. Lévy statistics and anomalous transport: Lévy flights and subdiffusion. *In* Encyclopedia of Complexity and Systems Science. R. Meyers, ed. Springer, pp. 5218–5239.

50. Weiss, M. 2014. Crowding, diffusion, and bichemical reactions. *Int. Rev. Cell. Mol. Biol.* 307:383–417.

51. Lenne, P. F., L. Wawrezinieck, …, D. Marguet. 2006. Dynamic molecular confinement in the plasma membrane by microdomains and the cytoskeleton meshwork. *EMBO J.* 25:3245–3256.

52. Malchus, N., and M. Weiss. 2010. Elucidating anomalous protein diffusion in living cells with fluorescence correlation spectroscopy-facts and pitfalls. *J. Fluoresc.* 20:19–26.

53. Lubelski, A., and J. Klafter. 2009. Fluorescence correlation spectroscopy: the case of subdiffusion. *Biophys. J.* 96:2055–2063.

54. Wachsmuth, M., W. Waldeck, and J. Langowski. 2000. Anomalous diffusion of fluorescent probes inside living cell nuclei investigated by spatially-resolved fluorescence correlation spectroscopy. *J. Mol. Biol.* 298:677–689.

55. Wu, J., and K. M. Berland. 2008. Propagators and time-dependent diffusion coefficients for anomalous diffusion. *Biophys. J.* 95:2049–2052.

56. Boon, J. P., and J. F. Lutsko. 2015. Nonlinear theory of anomalous diffusion and application to fluorescence correlation spectroscopy. *J. Stat. Phys.* 161:1366–1378.

57. Khadem, S. M. J., C. Hille, …, I. M. Sokolov. 2016. What information is contained in the fluorescence correlation spectroscopy curves, and where. *Phys. Rev. E.* 94:022407.

58. Szymanski, J., and M. Weiss. 2009. Elucidating the origin of anomalous diffusion in crowded fluids. *Phys. Rev. Lett.* 103:038102.

59. Metzler, R., and J. Klafter. 2000. The random walk's guide to anomalous diffusion: a fractional dynamics approach. *Phys. Rep.* 339:1–77.

60. Mantegna, R. N., and H. E. Stanley. 1994. Stochastic process with ultraslow convergence to a Gaussian: the truncated Lévy flight. *Phys. Rev. Lett.* 73:2946–2949.

61. Chen, K., B. Wang, and S. Granick. 2015. Memoryless self-reinforcing directionality in endosomal active transport within living cells. *Nat. Mater.* 14:589–593.

62. Chechkin, A. V., F. Seno, …, I. M. Sokolov. 2017. Brownian yet non-Gaussian diffusion: from superstatistics to subordination of diffusing diffusivities. *Phys. Rev. X.* 7:021002.

63. Chubynsky, M. V., and G. W. Slater. 2014. Diffusing diffusivity: a model for anomalous, yet Brownian, diffusion. *Phys. Rev. Lett.* 113:098302.

64. Weiss, M., H. Hashimoto, and T. Nilsson. 2003. Anomalous protein diffusion in living cells as seen by fluorescence correlation spectroscopy. *Biophys. J.* 84:4043–4052.

65. Schwille, P., J. Korlach, and W. W. Webb. 1999. Fluorescence correlation spectroscopy with single-molecule sensitivity on cell and model membranes. *Cytometry.* 36:176–182.

66. Bronshtein, I., E. Kepten, …, Y. Garini. 2015. Loss of lamin A function increases chromatin dynamics in the nuclear interior. *Nat. Commun.* 6:8044.

67. Hofling, F., K. Bamberg, and T. Franosch. 2011. Anomalous transport resolved in space and time by fluorescence correlation spectroscopy. *Soft Matter.* 7:1358–1363.

68. Wawrezinieck, L., H. Rigneault, …, P.-F. Lenne. 2005. Fluorescence correlation spectroscopy diffusion laws to probe the submicron cell membrane organization. *Biophys. J.* 89:4029–4042.

69. Destainville, N. 2008. Theory of fluorescence correlation spectroscopy at variable observation area for two-dimensional diffusion on a meshgrid. *Soft Matter.* 4:1288–1301.

70. Bag, N., X.-W. Ng, …, T. Wohland. 2016. Spatiotemporal mapping of diffusion dynamics and organization in plasma membranes. *Methods Appl. Fluoresc.* 4:034003.

71. Loverdo, C., O. Bénichou, …, R. Voituriez. 2008. Enhanced reaction kinetics in biological cells. *Nat. Phys.* 4:134–137.